Author's Accepted Manuscript

3D Morphology Design for Forward Osmosis

Meixia Shi, Galina Printsypar, Phuoc H.H. Duong, Victor M. Calo, Oleg Iliev, Suzana P. Nunes

Cite this article as: Meixia Shi, Galina Printsypar, Phuoc H.H. Duong, Victor M. Calo, Oleg Iliev and Suzana P. Nunes, 3D Morphology Design for Forward Osmosis, *Journal of Membrane Science*, http://dx.doi.org/10.1016/j.memsci.2016.05.061

3D Morphology Design for Forward Osmosis

Meixia Shi,[ab] Galina Printsypar,[bc] Phuoc H. H. Duong,[a] Victor M. Calo,[bd] Oleg Iliev,[be]

and Suzana P. Nunes[a,*]

[a] King Abdullah University of Science and Technology (KAUST), Biological and Environmental Sciences & Engineering Division (BESE), Thuwal 23955-6900, Saudi Arabia

[b] King Abdullah University of Science and Technology (KAUST), Center for Numerical Porous Media (NumPor), Thuwal 23955-6900, Saudi Arabia

[c] Weierstrass Institute for Applied Analysis and Stochastics, Berlin 10117, Germany

[d] Curtin University, Applied Geology Department, Western Australian School of Mines, Faculty of Science and Engineering, Perth, Western Australia 6845, Australia

[e] Fraunhofer Institute for Industrial Mathematics, Flows and Materials Simulation Department, Kaiserslautern 67663, Germany

*Corresponding author. suzana.nunes@kaust.edu.sa

Abstract

We propose a multi-scale simulation approach to model forward osmosis (FO) processes using substrates with layered homogeneous morphology. This approach accounts not only for FO setup but also for detailed microstructure of the substrate using the digitally reconstructed morphology. We fabricate a highly porous block copolymer membrane, which has not been explored for FO heretofore, and use it as the substrate for interfacial polymerization. The substrate has three sub-layers, namely a top layer, a sponge-like middle layer, and a nonwoven fabric layer. We generate a digital microstructure for each layer, and verify them with experimental measurements.

The permeability and effective diffusivity of each layer are computed based on their virtual microstructures and used for FO operation in cross-flow setups at the macro scale. The proposed simulation approach predicts accurately the FO experimental data.

Keywords: multi-scale simulation, digital membrane microstructure, concentration polarization, block copolymer substrate

Nomenclature

A pure water permeance

Δm mass enhancement

ρ density of water

a effective membrane area

Δt operational time for collecting water

ΔP applied pressure or pressure drop

R salt rejection

C_p sodium chloride concentration of the permeate solution

C_f sodium chloride concentration of the feed solution

B salt permeability coefficient

$\Delta\pi$ osmotic pressure difference across the membrane

J_w water flux in FO test

J_s salt flux in FO test

C_t sodium chloride concentration of the feed solution at the beginning

C_0 sodium chloride concentration of the feed solution at the end

V_t volume of the feed solution at the beginning

V_0 volume of the feed solution at the end

$\mathbf{U}$ velocity

μ viscosity

P pressure

K Darcy permeability

K_s Darcy permeability of the selective layer

Q flow rate

L thickness of the microstructure

D molecular diffusion

D_{eff} effective diffusivity

C concentration

ΔC concentration drop

μ_{eff} effective viscosity

$\mathbf{n}$ normal unit vector to the selective layer

l thickness of the selective layer

π osmotic pressure

1   Introduction

Water desalination by reverse osmosis is an essential technology due to the global water shortage in large parts of the world. Apart from seawater desalination, water reuse is needed to meet the water demand, opening opportunities for less established membrane technologies [1, 2], such as forward osmosis [3-6], nanofiltration [7-9], and membrane distillation [10-13].

Forward osmosis (FO) is an emerging membrane technique for water treatment [14], food processing [15], pharmaceutical industry [16], and other applications [17]. Typically, a thin-film composite membrane for FO is constituted by three layers [18]: a thin selective polyamide layer (dense top layer), a porous polymeric substrate (middle asymmetric layer with fine pores), and a fabric support layer (bottom layer with bigger pores and higher porosity). An important challenge for the development of FO membranes is the fabrication of polymer substrates, for deposition of the thin selective layer. These substrates should cause minimum resistance to the water flux, while minimizing the solute flux and the internal concentration polarization (ICP) during operation, as well as provide high mechanical stability. While the external concentration polarization is related to the solute concentration differences close to the membrane surface and the bulk of the solution, developed during operation, ICP occurs particularly in the membrane substrate. A concentration gradient is internally built, disturbing the osmotic pressure gradient, which is the main driving force for water transport through the membrane in the FO process.

Different materials have been investigated for FO substrates, such as polysulfone [19-21], polyethersulfone [22-24], polyacrylonitrile [25, 26], polyimide [27], and polytriazole-co-polyoxadiazole [28]. The nature of the chosen polymer controls the

hydrophilicity, which affects the water flow. Morphology minimized the internal concentration polarization, even more than the substrate chemical composition. The experimental optimization of membrane morphology for FO has been topic of investigation of very good groups in the field, using different approaches [29-31]. The most common morphologies of asymmetric membranes, sponge- and finger-like have been compared in [29]. Another approach is to use substrates constituted by electrospun fibers [24, 32]. High porosity contributes to low ICP and minimizes any detrimental effect on water flow. Large and open pores are preferred on one side of the substrate to minimize the concentration gradient. Small pores on the other side of substrate surface used for the deposition of the thin selective layer are preferred to guarantee its mechanical stability. The high substrate surface porosity is important to fully use the surface area of the thin selective layer, without adding any barrier for the continuous water flow through the multilayer membrane. A new class of porous asymmetric membranes, with exceptionally high pore density and narrow pore size distribution in the scale of ten to a few hundreds nm [33-35], is based on block copolymers. These membranes are prepared by taking advantage of the block copolymer capability of self-assembly in various patterns in solution. By combining self-assembly and the classical method of phase inversion by immersion in a non-solvent bath, highly ordered and highly porous membranes are obtained. Our group has been investigating this class of membranes for years, exploring it for ultra- and nanofiltration [36-39]. Challenging separations of proteins with similar sizes have been demonstrated under exceptional water permeance compared to other membranes of similar molecular weight cut-off [40]. The unique characteristics of block copolymer membranes suggest

that they could also be beneficial for FO application [41]. However, there is still no report evaluating block copolymer membranes as FO substrates. Hence, in this work block copolymer membranes are experimentally evaluated as substrates for FO membranes compared to polyethersulfone substrates, tested in the same conditions. For the preparation of FO membranes we deposit thin selective polyamide layers via interfacial polymerization (IP) on the top of isoporous block copolymer membranes with unique pore patterns.

Simulations of FO membrane performance

In this work, we exploit the regular surface pore morphology and high porosity offered by block copolymer membranes to demonstrate a new simulation approach. Using 3D simulations of membrane microstructure and experimental validation, we recently showed how the membrane morphology affects the water flux in ultrafiltration experiments [42]. Here we use analogous 3D digital microstructures and extend the simulation approach to predict the performance of FO membranes.

By changing the polymer, solvent, and other preparation conditions, innumerous morphologies can be experimentally obtained. Simulations that account for membrane microstructure can be helpful to narrow the variety of morphology patterns with most promising possibilities for success. In most reports experimental developments and simulations are treated separately. Only a few reports use 3D simulations (see detailed discussion below) and to the best of our knowledge none of the previous reports use simulations for 3D digital reconstruction of microscopic morphology coupled with the fluid flow and solute transport in the realistic cross-flow FO setup. Our approach properly predicts the performance of a proposed morphology.

Due to the nature of the FO processes, solute transport inside the membrane is diffusive and not convective. Therefore, effective diffusivity, which is the diffusivity of the solute inside a porous medium, defines the internal concentration polarization and, as a result, the membrane performance. The effective diffusivity has been previously studied using different modeling approaches. One of the approaches was proposed by Lee et al. [43] for pressure retarded osmosis and then extended by Loeb et al. [44] for forward osmosis. In these studies a macroscopic parameter, the membrane structural parameter, was introduced. The structural parameter lumps together several characteristics of the membrane such as thickness, tortuosity, and porosity. This structural parameter essentially represents membrane morphology at the macro scale. Later Tang et al. [45] and Park et al. [46] developed further this concept. However, the parameter in this method is fit using FO experiments assuming a certain approximation, since it cannot be computed directly. Moreover, the structural parameter lumps different characteristics of the support layer of a membrane into a single parameter, which restricts the mathematical model in case of asymmetric FO membranes and can introduce additional error into the simulation results. Alternatively, Ramon et al. in [47, 48] employed 2D and 3D micro-scale simulations to investigate how pore size and porosity of the support layer as well as thickness and roughness of the selective layer impact permeability and local distribution of solute and water fluxes. The mathematical model used in [47, 48] accounts only for diffusion inside the membrane without water flow while the effects of the external concentration polarization are modeled using a simplified geometrical representation of the membrane microstructure. The third approach to investigate microstructure of FO membranes was employed by Li et al. [49].

7

The authors used pore-network modeling to study the influence of microstructure of porous support on the internal concentration polarization, while the external concentration polarization was neglected and the microscopic morphology of the support was idealized. In general, most of the works concerned with the modeling of FO processes use an approximation of the effective diffusivity by molecular diffusion scaled with porosity of the membrane [45, 46, 50]. Since the diffusion dominates inside the FO membrane, a more accurate approximation of the effective diffusivity of membrane is needed.

In this study, we propose a multi-scale approach to model FO membranes with layered homogeneous morphology. Our approach accounts for realistic membrane microstructure and for full FO process in a cross-flow setup. First, at the micro scale we generate the digital membrane morphology for the block copolymer substrate and compute water permeance and effective diffusivity using the software tool GeoDict [51]. Since the membrane is asymmetric, the micro-scale simulations are performed for each layer (parallel to the surface), which composes the membrane support. Each layer is assumed to be homogeneous along the direction parallel to the membrane surface, without macroscopic heterogeneities. Then, using the software tool PoreChem [52], we perform FO simulations at the macro scale using parameters of the membrane obtained from the micro scale. The simulation results are verified using FO experiments performed with newly developed block copolymer membranes coated by interfacial polymerization.

2 Materials and methods

2.1 Materials

Poly(styrene-*b*-4-vinyl pyridine) block copolymers (PS-*b*-P4VP, M_n=188000-*b*-64000, M_w/M_n=1.16) were purchased from Polymer Source, Inc. Polyethersulfone Ultrason® E 6020 P (PES, M_w=75 000 g/mol, M_w/M_n=3.4) was obtained from BASF. Polyester nonwoven was purchased from Sojitz Europe plc (made by Hirose Paper). Polyester Woven Mesh WS0050-60P was purchased from Industrial Netting, Inc. Filter papers were purchased from GE Whatman. Trimesoyl chloride (TMC) and m-phenylenediamine (MPD), N, N-dimethylformamide (DMF), acetone, 1,4-dioxane (DIOX) and hexane were purchased from Sigma-Aldrich Corporation and used as received. We used Milli-Q ultrapure water for all the tests and conducted all experiments at room temperature of approximately 22°C except further instructions.

The FO membranes in this work were formed by three layers: (i) a rough support with open porosity, constituted by a polyester woven or nonwoven; (ii) an asymmetric porous substrate, which was made of PS-*b*-P4VP or PES and (iii) a polyamide layer prepared by interfacial polymerization.

2.2 Substrate fabrication

The asymmetric porous substrate was prepared by phase inversion: polymer solution casting followed by immersion in water. As mentioned above the two polymers used for the substrate were PES and PS-*b*-P4VP. The PES casting solution contained 18 wt% polymer and 82 wt% DMF. The PS-*b*-P4VP solution had 18 wt% polymer, 16 wt% acetone, 24 wt% DMF and 42 wt% DIOX. The polymer solutions were stirred overnight at room temperature. Before casting, a nonwoven was firstly fixed on a clean glass plate

using adhesive tape. Then the solution was poured onto the nonwoven, and spread with a casting knife with a gate gap of 250 μm, excluding the nonwoven thickness. For the block copolymer substrate a solvent evaporation time of 10 seconds was allowed before the immersion into the water bath. The obtained asymmetric porous substrates were stored in water before further characterizations or modifications.

2.3 Selective layer fabrication via interfacial polymerization (IP)

The selective layers of the FO membranes were prepared by the interfacial polymerization between MPD and TMC monomers on PS-*b*-P4VP and PES porous substrates. They are here referred as PS-*b*-P4VP/IP and PES/IP membranes, respectively. Let us briefly explain the fabrication process of the elective layer. First, the substrate was immersed in 2 wt% MPD water solution for 2 minutes; then, the solution was discarded, and the remaining solution droplets on the membrane surface were removed with a filter paper. Later, a frame was used to assemble the membrane so that only the top surface of the substrate was exposed, and 0.1 wt% TMC in hexane solution was poured into the frame to react with MPD on the substrate surface for 1 minute. After draining the TMC solution, the membrane was left in the air for 1 minute more and finally the membrane was rinsed with water to wash out the unreacted monomers, and stored in water for further tests.

2.4 Membrane characterizations

2.4.1 Field emission scanning electron microscopy (FESEM)

The membrane morphology was imaged using Nova Nano 630 or Quanta 600 FEI field emission scanning electron microscopes. The samples were freeze-dried, and

subsequently coated with 3 nm iridium using Q150T sputter coater (Quorum Technologies). For cross section samples, the membranes after freeze-drying were fractured in liquid nitrogen.

2.4.2 Atomic force microscopy (AFM)

The membrane surface roughness was characterized on an Agilent 5400 Scanning Probe Microscope (Agilent Technologies, Inc.). The freeze-dried samples with areas of 3 μm × 3 μm were scanned using tapping mode.

2.4.3 Contact angle measurement

The contact angle (θ) was measured on a Krüss Easy Drop (Krüss GmbH) equipment. A water droplet with a constant volume of 1μL was dropped onto the membrane surface in the static mode, and then an image was taken to calculate the contact angle.

2.4.4 Permeance of the substrates

The water permeance of the substrate was measured in the dead-end filtration mode. The measurement was conducted in an Amicon Stirred Cell Model 8010 connected to a large deionized water tank with an effective membrane area of 4.1 cm^2 under a trans-membrane pressure of 1 bar. Pure water permeance A was calculated using the following equation

$$A = \frac{\triangle m}{\rho \times a \times \triangle t \times \triangle P}. \tag{1}$$

Here, Δm is the mass enhancement in the period of Δt; ρ is the density of water; a is the effective membrane area; ΔP is the applied pressure.

11

The gas transport property of the nonwoven fabric support was measured using the setup introduced in [53]. The thickness was estimated by the thickness gauge. Finally, the nonwoven fabric's permeability was calculated by Darcy's law.

2.4.5 Porosity of the substrates

The porosity of the polymeric substrate was measured using the dry-wet method, and more detailed is available in our previous work [42]. Additionally, the nonwoven fabric's porosity was measured by the mercury porosimetry using the standard method.

2.4.6 Mass transport characteristics of membranes with IP layer

The water permeance of membranes coated by interfacial polymerization was tested in a dead-end cell, constructed at KAUST, suitable for high pressure experiments (8 bar in these experiments), using deionized water as feed and an effective membrane area of 3.8 cm^2. The water permeance was calculated based on Equation (1).

The salt rejection of membranes coated with the IP layer was measured using a similar method with 2000 ppm sodium chloride solution as feed, under a stirring speed of 600 rpm. After filtration, both feed and permeate solutions conductivity values were measured using a conductivity meter Cond 3210 (WTW GmbH, Germany). We calculate the salt rejection R using Equation (2).

$$R = 1 - \frac{C_p}{C_f} \times 100\%, \tag{2}$$

where C_p and C_f are the sodium chloride concentrations of the permeate and the feed solutions, respectively, based on the measured conductivity values.

The salt permeability coefficient B was determined by Equation (3) according to the solution-diffusion theory [54].

12

$$\frac{1-R}{R} = \frac{B}{A \times (\Delta P - \Delta \pi)}, \tag{3}$$

where ΔP and $\Delta \pi$ are the pressure difference and osmotic pressure difference across the membrane, respectively.

2.5 FO performance tests

We used a lab-scale FO setup to test the performance of the FO membranes including the water and salt fluxes [55]. The dimensions of the FO cell (plate-and-frame) were 2 cm in length, 1 cm in width, and 1 mm in height. All tests were operated using counter-current cross flow with the flow rate of 200 mL/min for each channel. The feed and draw solution reservoirs had a capacity of 900 mL. The membranes were tested in FO mode and PRO mode. The FO mode is characterized by the membrane's selective layer facing the feed solution; in the PRO mode, the selective layer faces the draw solution. In the performed tests, the feed was water; the draw solution contained 2 M sodium chloride. Due to the osmotic pressure difference, water flows from the feed to the draw solution side. The water flux was recorded using a computer connected to a balance, which reflected the weight change of the draw solution. The salt flux was monitored by a conductivity meter immersed in the feed solution. The water and salt flux were calculated using Equations (4) and (5), respectively.

$$J_w = \frac{\Delta m}{\rho \times a \times \Delta t}, \tag{4}$$

where J_w is the water flux across the membrane; Δm is the water (mass) collected within the period Δt; ρ is the density of water; and a is the effective membrane area.

$$J_s = \frac{C_t \times V_t - C_0 \times V_0}{a \times \Delta t}, \tag{5}$$

13

where J_s is the salt flux across the membrane; C_t and C_0 are the sodium chloride concentration of the feed solution at the beginning and the end of the measurement, respectively, based on the measured conductivity values; V_t and V_0 are the volumes of the feed solution at the beginning and the end of measurement, respectively. The reported data, including water and salt fluxes, were average values measured at 30 minutes after the experiment started.

3 Multi-scale models for FO

3.1 Micro-scale modeling

Based on available characterization of the membrane, such as FESEM images, porosity, and pore size distribution, we virtually generate the membrane microstructure applying different algorithms available in GeoDict (for more details see [51]). Then, we compute the intrinsic permeability and effective diffusivity for the digital microstructure of each layer. The permeability for a single layer or cumulative for several layers is compared with the experimental data to verify the obtained microstructure.

To compute the water permeability, we solve the Stokes system of equations, which reads

$$-\mu\nabla^2\mathbf{U} + \nabla P = 0, \qquad \nabla \cdot \mathbf{U} = 0; \tag{6}$$

where $\mathbf{U}$ is the velocity, μ is the viscosity, P is the pressure. The system of Equation (6) is supplemented by periodic boundary conditions in the direction tangential to the flow and either periodic boundary conditions with a constant pressure drop or inflow velocity and outflow pressure boundary conditions in the direction of the flow. The macroscopic Darcy vertical permeability is computed using volume averaged quantities as follows

14

$$K = -\frac{Q\mu L}{a\Delta P}; \tag{7}$$

where K is the permeability in the chosen flow direction; Q is the flow rate; L is the thickness of the microstructure; a is the area; ΔP is the pressure drop.

The effective diffusivity D_{eff} is a macroscopic quantity introduced to describe diffusion through the pore space of porous media. We compute the effective diffusivity for the given digital microstructure using mathematical modeling [51]. The diffusion in the pores is modeled by the Laplace equation

$$D\nabla^2 C = 0; \tag{8}$$

where D is the molecular diffusion, C is the concentration. We use Neumann boundary conditions on the pores walls, which are solid boundaries. The Neumann boundary conditions guarantee the gradient of the concentration in the normal direction to the solid boundaries to be zero and, therefore, zero solute flux though the solid boundaries. We use periodic boundary conditions in the direction tangential to the concentration gradient. The concentration gradient itself is modeled by a concentration difference on the two opposite faces of the structure. The macroscopic effective diffusivity D_{eff} is computed at a post-processing step

$$D_{eff} = \frac{J_s L}{a\Delta C}; \tag{9}$$

where J_s is the total solute flux in the direction from the draw solution to feed solution, ΔC is the concentration drop.

3.2 Macro-scale modeling

After we define the permeability K and the effective diffusivity D_{eff} of the support layer, we use these parameters as input data for the forward osmosis cross-flow model.

15

To model the fluid flow in the cross-flow channels and in the membrane we use the steady Navier-Stokes-Brinkman system of equations

$$-\nabla \cdot \left(\mu_{eff} \nabla \mathbf{U}\right) + (\rho \mathbf{U} \cdot \nabla)\mathbf{U} + \mu K^{-1}\mathbf{U} = -\nabla P, \tag{10}$$

$$\nabla \cdot \mathbf{U} = 0; \tag{11}$$

where μ_{eff} is the effective viscosity. K is the permeability in the porous medium and $K^{-1} = 0$ in the cross-flow channels. In general, the permeability is a tensor quantity, but here we consider a scalar quantity instead. This is enough for FO modeling as the membrane is dense and the flow inside the membrane occurs mainly in one direction. The solute transport is modeled using the following convection-diffusion equation

$$-\nabla \cdot (D\nabla C) + \nabla \cdot (\mathbf{U}C) = 0. \tag{12}$$

Here D is the molecular diffusion inside the cross-flow channels and $D \equiv D_{eff}$ inside the membrane. The selective layer is modeled using the following interfacial conditions

$$J_w = -\frac{K_s}{\mu\, l}(\Delta P - \Delta\pi(C)), \tag{13}$$

$$J_s = -B\Delta C; \tag{14}$$

where J_s is the solute flux through the selective layer, $J_w = \mathbf{U} \cdot \mathbf{n}$ is the water flux across the selective layer, $\mathbf{n}$ is the normal unit vector to the selective layer, l is the thickness of the selective layer, K_s is the water permeability of the selective layer, B is the solute permeability of the selective layer, operator Δ defines the drop of a quantity across the selective layer, π is the osmotic pressure as a function of the concentration.

4 Results and discussion

16

4.1 Characteristics of substrates

Both PS-*b*-P4VP and PES substrates were cast onto a 161 μm thick nonwoven fabric layer using 18 wt% polymer solution without any additive by nonsolvent induced phase inversion. PES was chosen for the comparison because it is one of the most used polymer for asymmetric porous membranes and can be seen as a standard system. The hydrophilicities of PS-*b*-P4VP and PES substrates are similar. As can be seen in Table 1, the contact angles of PS-*b*-P4VP and PES substrates are 72° and 67°, respectively. However, the two substrates strongly differ in morphology. The PS-*b*-P4VP substrate was prepared by self-assembly to form a highly ordered surface pore distribution with pore size around 40 nm as shown in Figure 1(a). Compared to the PES substrate surface (Figure 1(b)), the PS-*b*-P4VP substrate surface has a more uniform pore distribution and higher pore density. The cross sectional images in Figure 1 show that the PS-*b*-P4VP substrate exhibits a highly porous sponge-like structure with well-connected pores, while the PES substrate used here contains finger-like macrovoids. The large surface pore size, high porosity, and well inter-connected structure make the PS-*b*-P4VP substrate favorable for water transport. Hence, the PS-*b*-P4VP substrate has much higher pure water permeance measured as being 659 L m^{-2} h^{-1} bar^{-1}, compared to the PES substrate, for which the pure water permeance was 199 L m^{-2} h^{-1} bar^{-1} (Table 1). The surface topologies of the two substrates were confirmed by AFM as shown in Figure 2. The surface roughness of the substrates is presented as the root mean square height S_q and the arithmetic mean height S_a. PS-*b*-P4VP and PES substrates exhibit smooth surfaces with the surface roughness of approximately 5 nm. The AFM results clearly confirm that the PS-*b*-P4VP substrate has larger surface pore

size and higher surface porosity. The results suggest that the PS-*b*-P4VP substrate exhibits more favorable properties to be used as a support for the deposition of a thin polyamide layer to form a high performance FO membrane.

Table 1. Pure water permeance and contact angle of porous substrates

Substrate	Pure water permeance (L m^{-2} h^{-1} bar^{-1})	Contact angle (°)
PS-*b*-P4VP	659 ± 1	72 ± 3
PES	199 ± 12	67 ± 2

Surfaces

500 nm

Cross sections

50µm

25 µm

(a) PS-*b*-P4VP substrate   **(b) PES substrate**
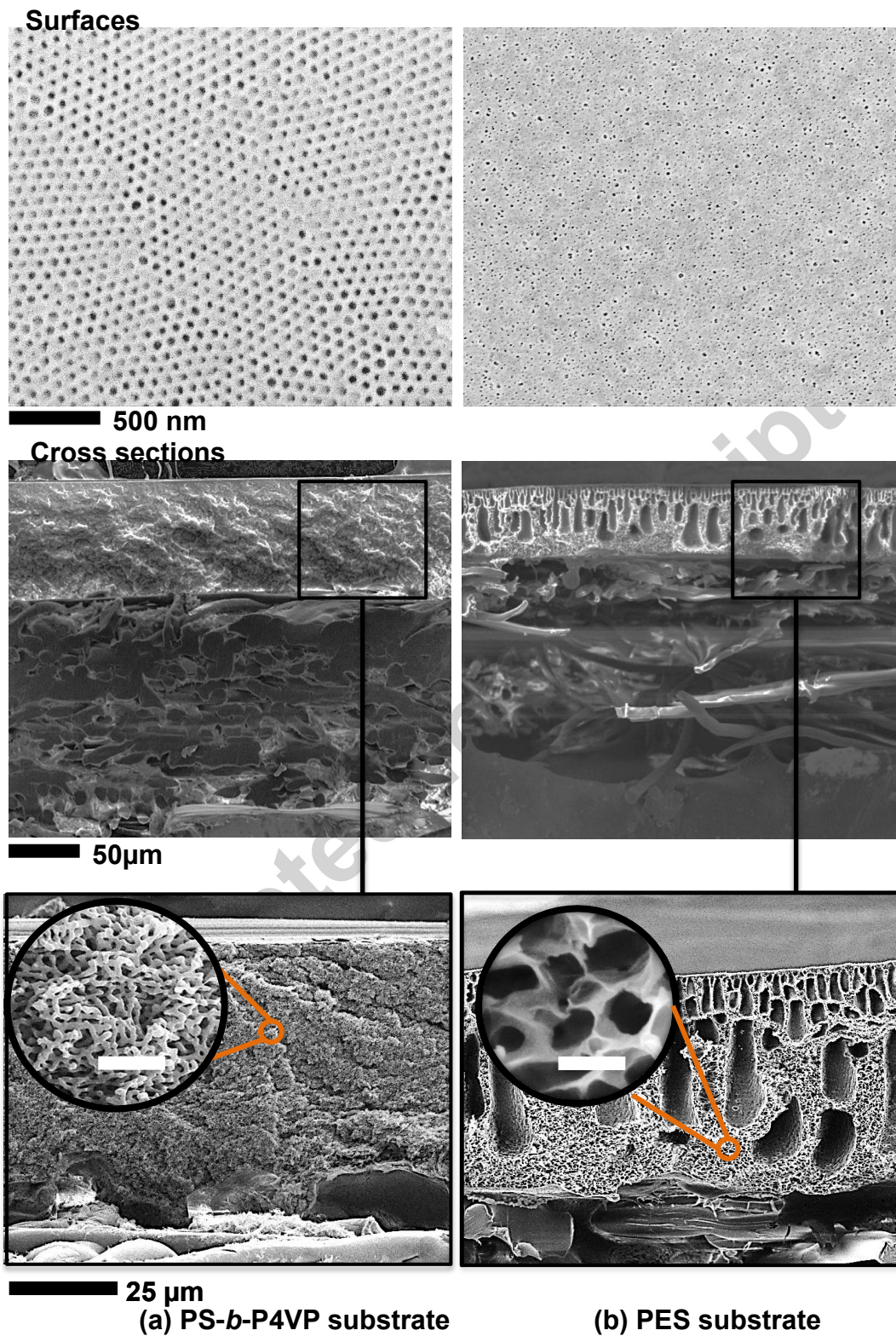
Figure 1. FESEM images of surfaces and cross sections of (a) PS-*b*-P4VP and (b) PES substrates.

19
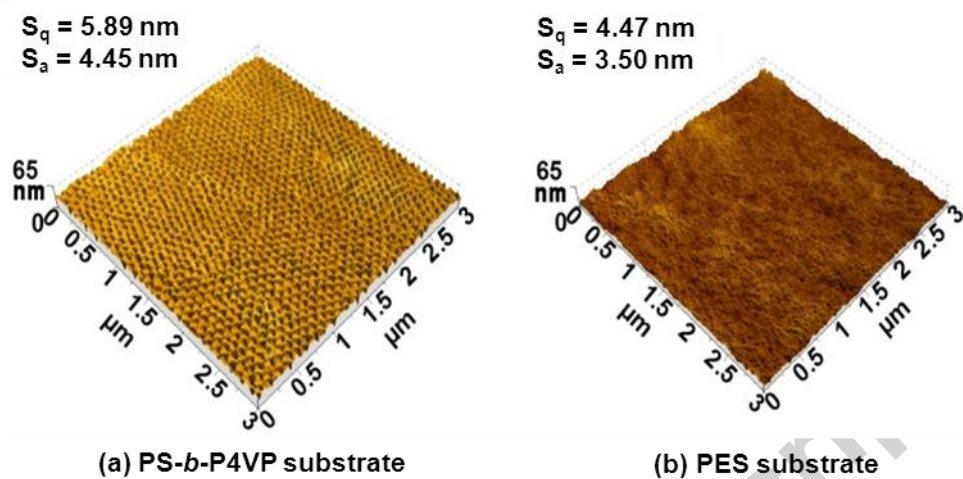
Figure 2. AFM images of (a) PS-*b*-P4VP and (b) PES substrates. S_a and S_q are the average roughness and root mean square roughness.

4.2 Characteristics of FO membranes

Figure 3 shows the morphology of surfaces and cross sections of substrates after coating with interfacial polymerization (PS-*b*-P4VP/IP and PES/IP). The IP surface on a PS-*b*-P4VP substrate has smaller and more regular spherical nodules while the structures on the PES substrate have larger features with more irregular shapes. The IP layer's thickness on PES substrate (~ 345 nm) is higher than on PS-*b*-P4VP (~ 91 nm). The AFM images are consistent with the FESEM observations regarding the shape and size of the IP layer features. The average roughness is around 14 nm for PS-*b*-P4VP/IP membrane and 65 nm for PES/IP membrane. This is the first time that block copolymer membranes are used as the substrate for interfacial polymerization. We observe that

the morphology of the surface on PS-*b*-P4VP/IP membrane reflects the isoporous morphology of the substrate.

The formation of the IP layer is highly influenced by the morphology and hydrophilicity of the substrate, as demonstrated by previous work of our group with the inclusion of a dense and hydrophilic intermediate layer of cellulose on hydrophobic and porous substrates [56]. Observations by other groups on different substrates also confirm the importance of porosity and hydrophilicity [57, 58]. In this work the hydrophilicity of both substrates is similar, as indicated by contact angle values in Table 1. Therefore, the primary effect is the substrate morphology, as well as the chemical interaction between the dissolved monomer (MPD) and the porous substrate. The block copolymer support has extremely high porosity with regular pore sizes and shapes. The pores have pyridine exposed for interaction with MPD. On the other hand, PES substrates, like almost all commonly available phase inversion membranes, have irregular pores with broad pore size distribution and different pore shapes. Interfacial polymerization takes place at the interface between the substrate soaked with MPD aqueous solution and the TMC dissolved in hexane, which is immiscible with the water phase. The monomers immediately react forming a thin polyamide layer. Interfacial instabilities contribute to form the layer with the typical morphology seen on PES substrate in Figure 3(b). The local heat generation resulting from the polymerization reaction itself is claimed to induce convection and lead to the rough topology [59, 60]. But we believe that the substrate morphology and the monomer distribution and availability on the substrate surface are at least as important as the local heat. When PES substrate is used, the reaction between monomers preferentially takes place in the

irregularly shaped pore areas where the MPD freely contacts the TMC monomer. The exothermic reaction contributes even more to the fast MPD transfer out of the pores leading to the rough morphology. In the case of the PS-*b*-P4VP substrate, the pore density is higher, and the chemical composition of the substrate with pyridine groups might also favor a better distribution of the diamine monomer on the surface. The reaction occurs with less convection or interface instability. Therefore, the roughness is lower for the PS-*b*-P4VP substrate than for PES, as confirmed in Figure 3.

Surfaces

$S_q = 14.3$ nm $S_a = 7.82$ nm

$S_q = 64.9$ nm $S_a = 49.2$ nm

2 µm

Cross sections: Interfaces

91 nm

345 nm

2 µm

(a) PS-*b*-P4VP /IP membrane   (b) PES/IP membrane
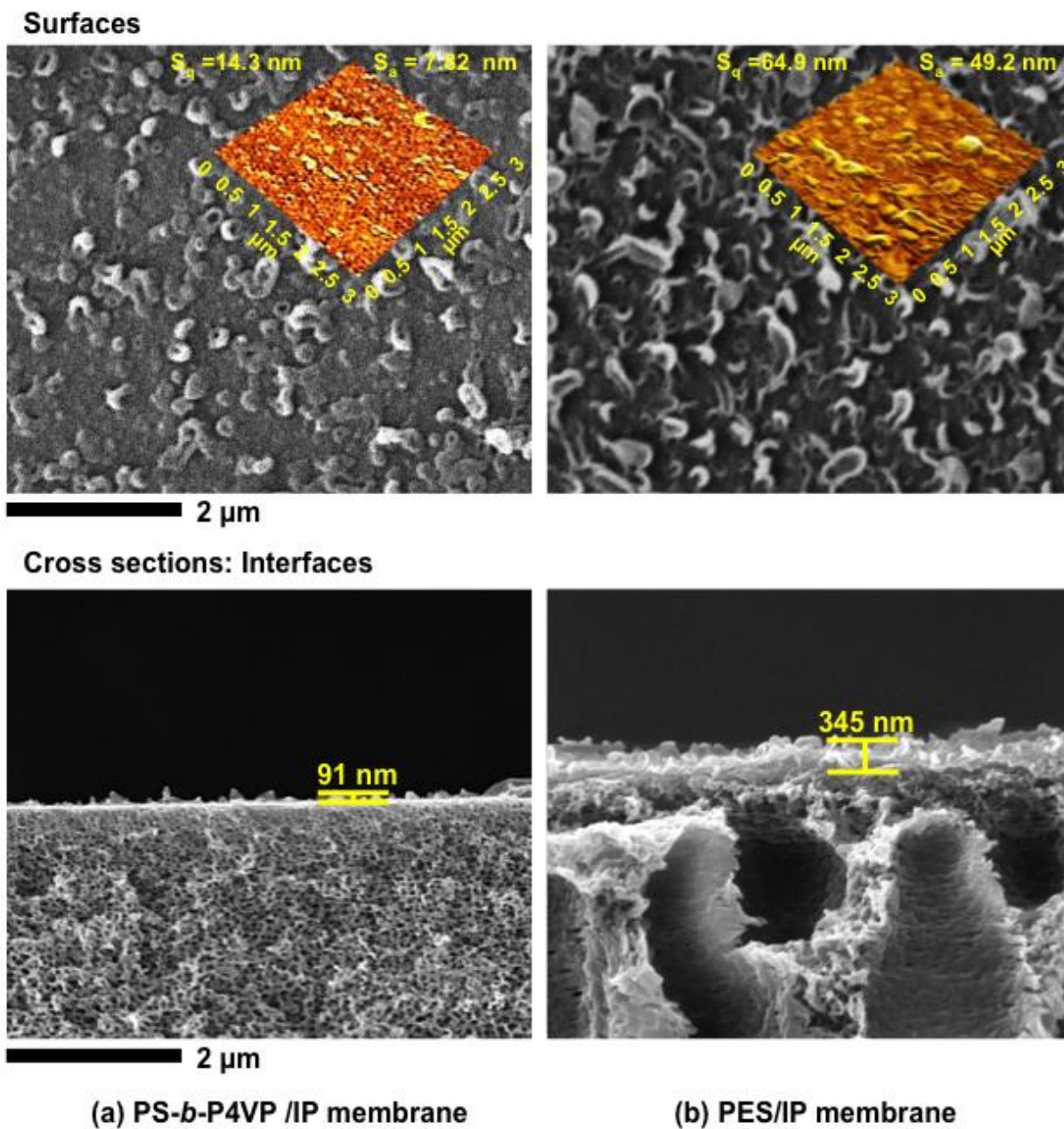
Figure 3 FESEM images of surfaces and cross sections of membranes after interfacial polymerization on (a) PS-b-P4VP and (b) PES substrates; Inset: AFM of each surface. Sa and Sq are the average roughness and root mean square roughness, respectively.

The transport properties of PS-*b*-P4VP/IP and PES/IP membranes under hydrodynamic pressure are listed in Table 2. Both membranes have good salt rejection values above 90%. The PS-*b*-P4VP/IP membrane has even lower salt permeability coefficient. The transport properties indicate the suitability of the two membranes to be used in FO processes. The water permeance for PS-b-P4VP/IP is lower than for PES/IP, although the permeance of the substrate without the IP layer is more than 3-fold higher. This indicates that the IP layer is formed with different characteristics. The IP layer on PS-*b*-P4VP is smoother and has a lower effective surface area, justifying the lower permeance. But as we see below, the pore morphology of the substrate contributes much more to the FO performance than the permeance of the selective layer.

Table 2 Transport properties of PS-*b*-P4VP/IP and PES/IP membranes

| Membrane	Pure water permeance A^a (L m^{-2} h^{-1} bar^{-1})	Rejection R^b (%)	Salt permeability coefficient B (L m^{-2} h^{-1})
PS-*b*-P4VP/IP	0.30 ± 0.02	91.2 ± 5.3	0.19 ± 0.12
PES/IP	0.63 ± 0.03	94.2 ± 3.6	0.26 ± 0.16

^{a}Pure water permeance A measured under 8 bar.

^{b}Rejection R measured under 8 bar using 2000 ppm sodium chloride solution as feed.

FO tests for PS-*b*-P4VP/IP and PES/IP membranes were conducted using deionized water as feed and 2M NaCl as draw solution. The results are shown in Figure 4. Compared to PES/IP membranes, PS-*b*-P4VP/IP membranes exhibit higher water flux in both membrane orientations (FO and PRO modes) and also slightly higher salt flux. PS-*b*-P4VP/IP membrane has thinner IP layer and a more porous substrate with good interconnectivity. These characteristics lead to less internal concentration polarization during the FO operation. Hence, the FO performance of PS-*b*-P4VP/IP membrane is higher than that of PES/IP.

In most experiments described above a thick nonwoven polyester fabric (161 μm thickness) was used as bottom support layer for the substrate. This fabric is normally used in industrial applications to increase the mechanical stability of membranes where the polyester fabric does not affect much the membrane performance in terms of water flux in applications for which hydrodynamic pressure is the driving force. However, in forward osmosis a thick and dense fabric contributes to internal concentration polarization and makes FO performance worse. Therefore, PS-*b*-P4VP/IP membranes were later prepared using a thinner woven fabric with more open porosity (mesh size of 50 μm and thickness of 60 μm). The results with the new membranes are shown in Figure 4. The FO water flux was almost twice increased in FO mode, and around 20% in PRO mode. Meanwhile, an increase of salt flux was also observed, indicating the presence of defects in the polyamide layer, which was formed on a rougher and thinner substrate layer prepared with an open woven fabric.
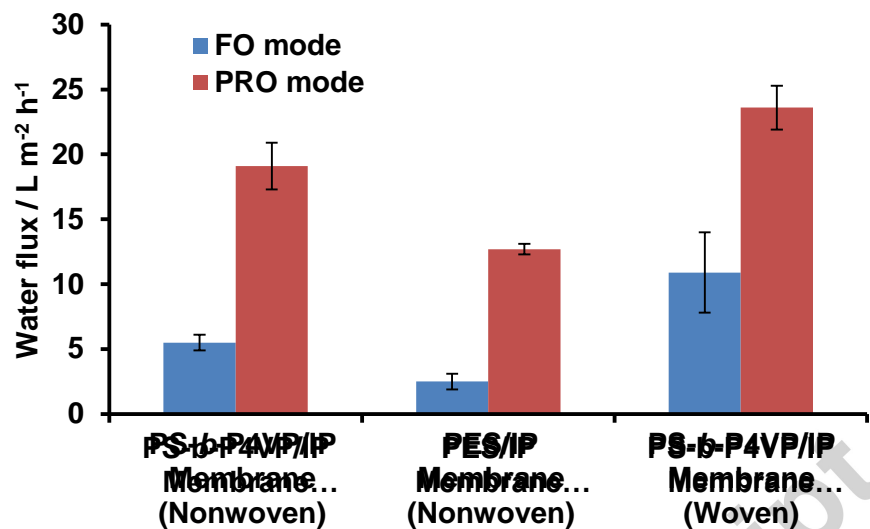
(a)
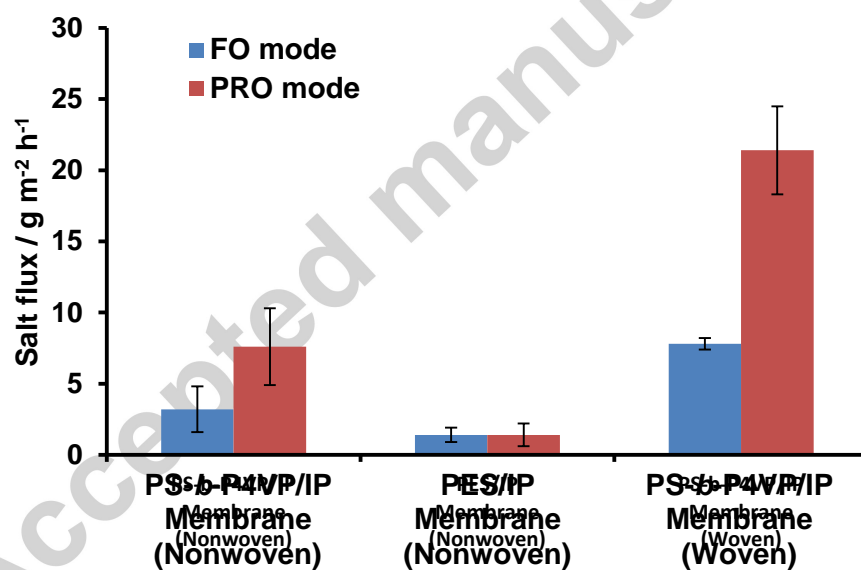
(b)

Figure 4. (a) Water and (b) salt fluxes in FO and PRO modes.

4.3 Digital membrane morphology

We used a micro-scale simulation approach to model the PS-*b*-P4VP membrane. We observed from the FESEM images in Figures 5 and 6 that the PS-*b*-P4VP substrate

26

has a denser layer on top and a homogeneous sponge-like microstructure far from the surface. Thus, we considered the substrate to consist of three layers: (1) top layer, (2) sponge-like middle layer, and (3) nonwoven support at the bottom, as depicted in Figure 8. Layer 1 includes both the top patterned regular pores and the sponge-like structure immediately below them.

Using the measured characteristics and the FESEM images, we digitally reconstructed the microstructure of each layer. Figures 5-7 show FESEM images of each layer together with their digital prototypes, respectively. Table 3 shows the measured characteristics of the real PS-*b*-P4VP substrate and the calculated characteristics of each layer. For the real PS-*b*-P4VP substrate we could measure only cumulative characteristics for layers 1 and 2 together, while in the simulation we reproduced each layer separately and computed separately all characteristics, such as permeability K and effective diffusivity D_{eff}. The effective diffusivity was not available from experiments, but is important for the FO performance. Figure 8 summarizes each layer and presents their 3D digital prototype, respectively.
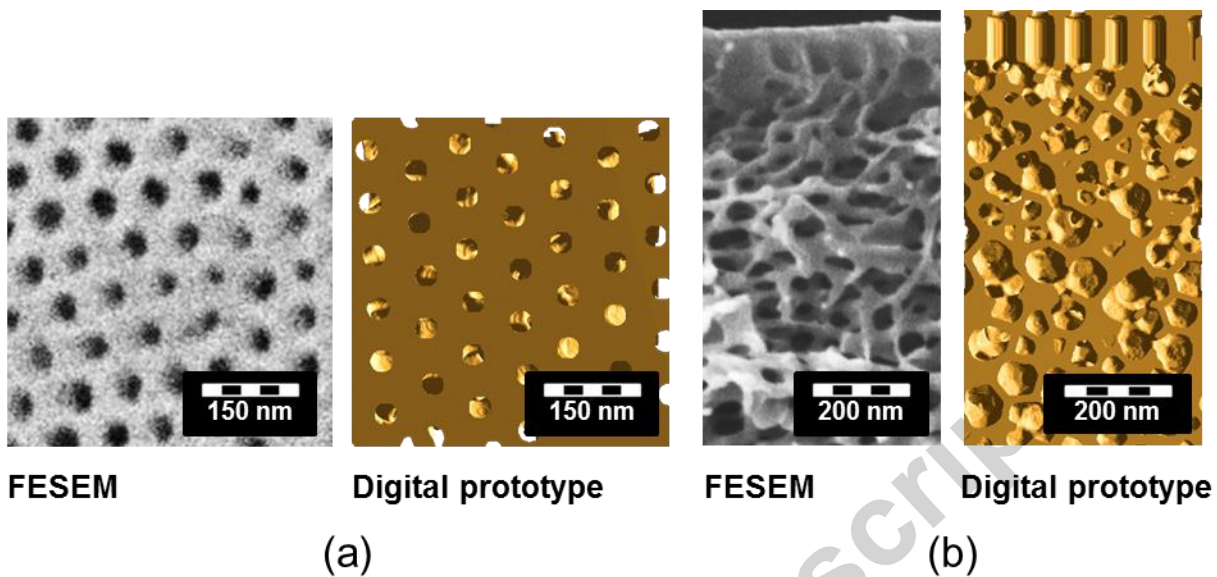
Figure 5. FESEM image and digital prototype of the denser top layer (1): (a) surface and (b) cross section view.
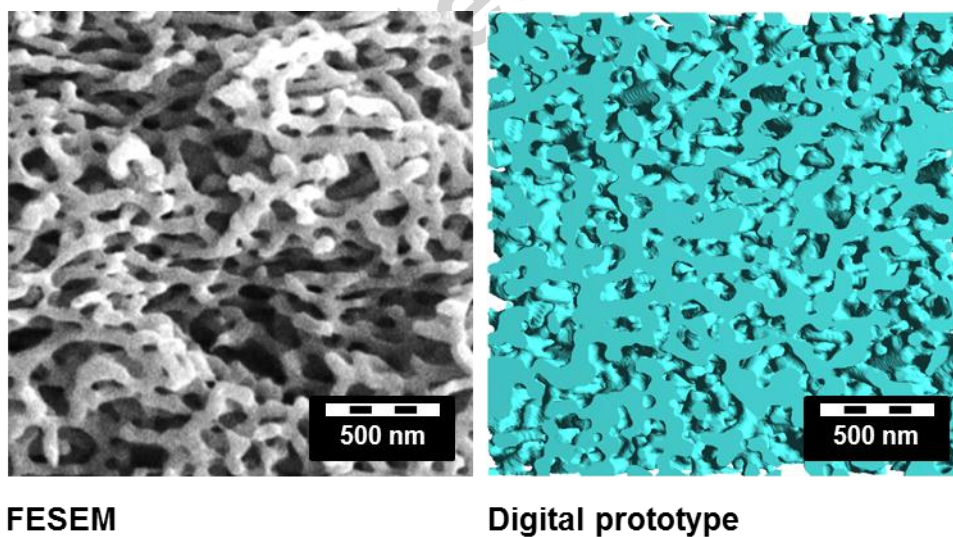

Figure 6. FESEM cross-section image and digital prototype of the sponge-like middle layer (2).

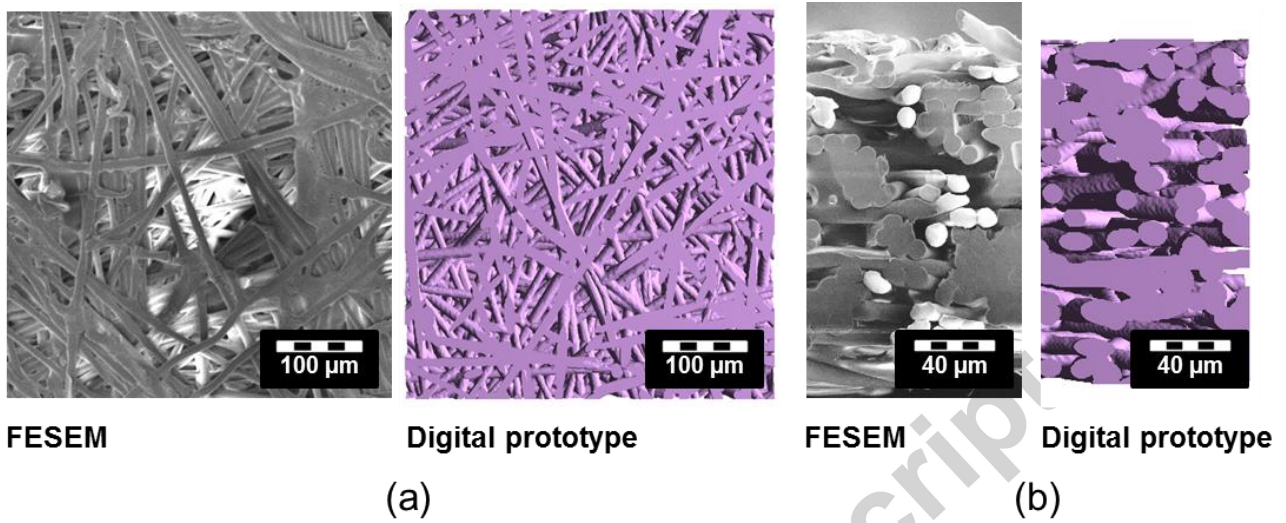**FESEM**   **Digital prototype**   **FESEM**   **Digital prototype**

(a)   (b)

Figure 7. FESEM (a) surface and (b) cross-section images and the corresponding digital prototypes of the nonwoven fabric (layer 3).

Table 3. Properties of the PS-*b*-P4VP substrate layers

Layer	Thickness (µm)		Porosity (%)		Surface porosity (%)		Permeability (m^2)		Diffusivity (%)	
	Exp.[a]	Num.[b]	Exp.	Num.	Exp.	Num.	Exp.	Num.	Exp.	Num.
#1	--	2.5	--	66.8	18	18.8	--	1.63×10^{-17}	--	17.5
#2	--	65.5	--	66.2	--	--	--	1.53×10^{-16}	--	43.5
#1+#2	68	68	64.0	66.2	--	--	1.25×10^{-16}	1.17×10^{-16}	--	--
#3	161	161	57.7^c	54.9	--	--	1.31×10^{-12}	1.12×10^{-12}	--	27.4

^{a}Exp.: data experimentally obtained

^{b}Num.: data obtained from or applied in the simulation

^{c}Nonwoven fabric porosity is 57.7% measured by mercury porosimetry and 49.8% measured by the wet-dry method.
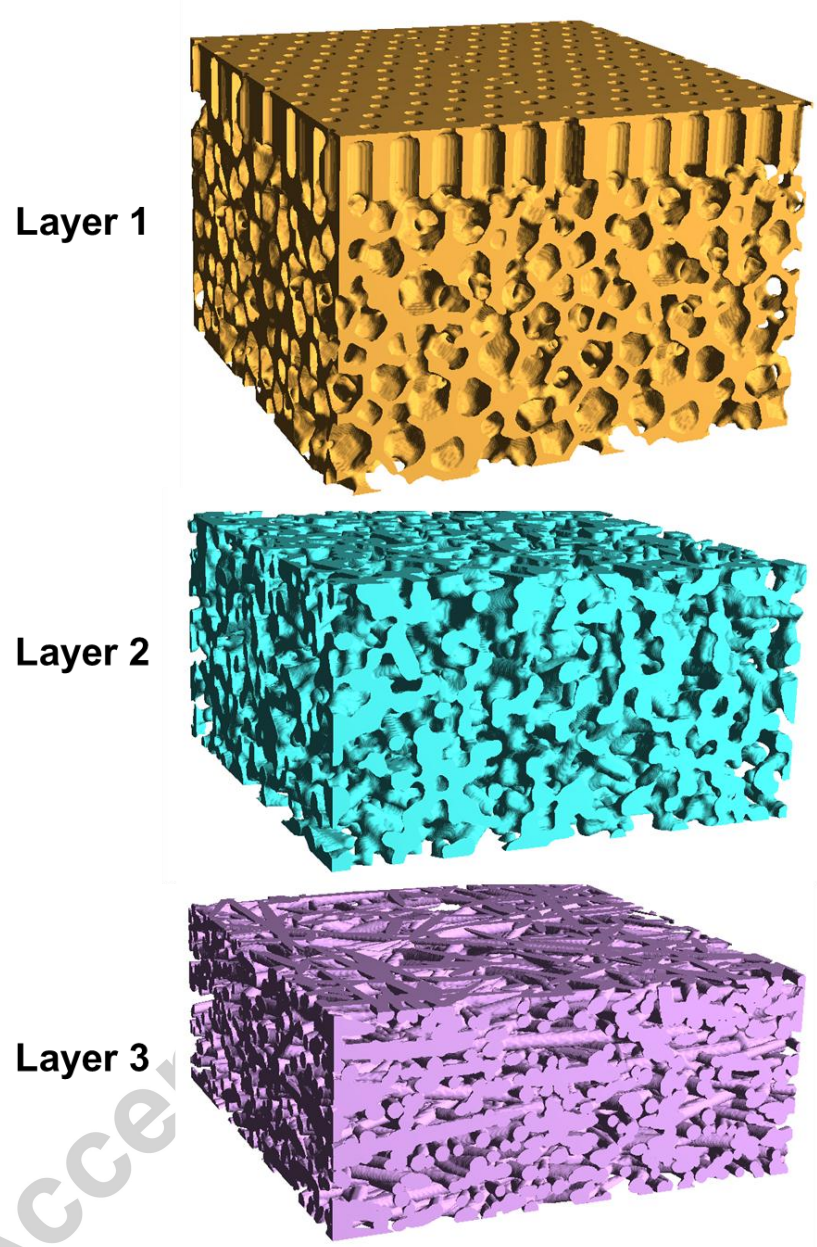
Layer 1

Layer 2

Layer 3

Figure 8. 3D digital substrate layers.

4.4 FO cross flow simulations

After we obtained all necessary parameters, mainly the permeability K and effective diffusivity D_{eff}, for all three layers from the micro-scale simulations, we run macro-scale FO simulations. The substrate was composed of three layers; each layer was considered as a homogenized porous medium; the selective layer was modeled by interfacial conditions. First, we run simulation in FO mode and fit the unknown water and solute permeabilities of the selective layer, K_s and B respectively. Then, we changed the membrane orientation and predicted the FO performance in the PRO mode using the obtained parameters. For the simulations, we used 2D counter-current cross flow setup (see Figure 9). The permeability K and effective diffusivity D_{eff} for the three homogenized layers are shown in Table 3. All other numerical parameters used in the simulations are presented in Table 4.
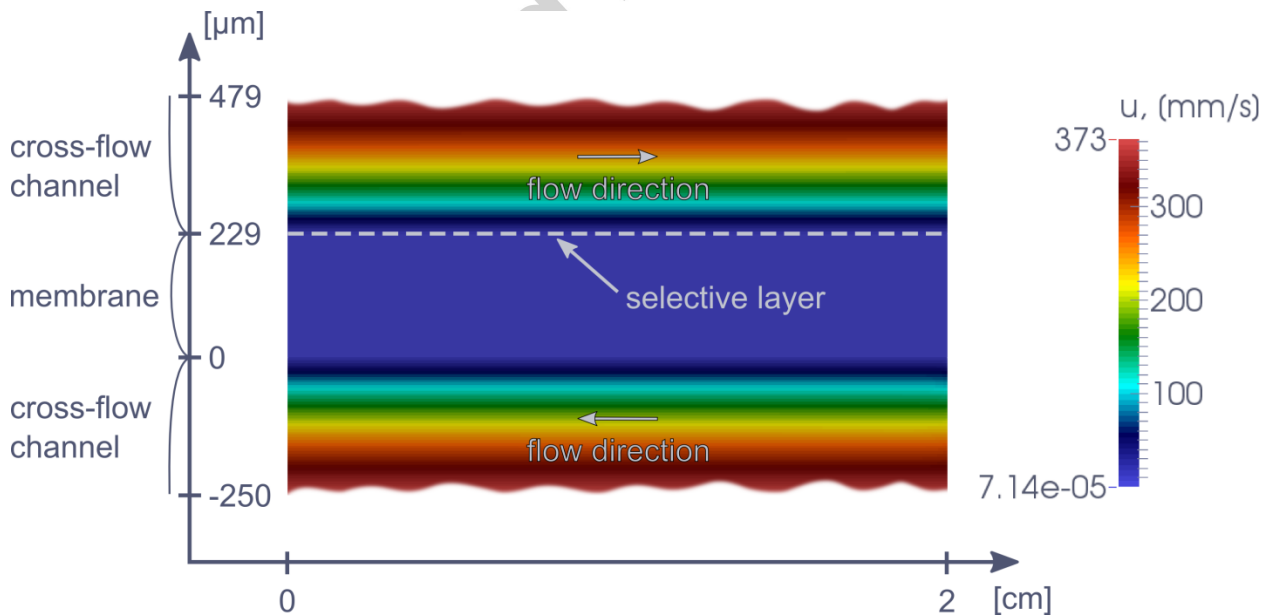

Figure 9. Velocity distribution in 2D counter-current cross flow FO setup.

Table 4. Input parameters for the macro-scale FO experiment

Parameter	Unit	Value
Density ρ	[kg/m^3]	988.207
Viscosity μ	[Pa s]	0.001002
Flow rate in the cross-flow channels	[L/min]	0.2
Heights of the cross-flow channels	[mm]	1
Length of the cross-flow channels	[mm]	20
Concentration in the draw channel	[M]	2
Concentration in the feed channel	[M]	0
Molecular diffusion D in Ω_f	[mm^2/s]	0.001
Water permeability of the selective layer K_s	[m^2]	6.48×10^{-23}
Solute permeability of the selective layer B	[m/s]	3×10^{-8}
Thickness of the selective layer s	[nm]	90
Osmotic pressure π	[KPa]	$379.8C^2 + 4260C$

Figure 9 shows the counter-cross flow setup and obtained velocity distribution. Figure 10 shows the concentration distributions in the FO and PRO mode. To show internal and external concentration polarization, the computational domain is split in three regions, namely the top cross-flow channel, the membrane, and the bottom cross-flow channel. In each region concentration distribution has its own color legend (on the

right side in the figure). Figure 11 shows the simulated water and salt fluxes in comparison with the experimental ones. A good match between experiments and simulations was obtained with an error around 10%. One source of the error is the reduction of the problem dimensionality. In macro-scale simulations we consider only 2D setup and neglect the shape of the cell element. Another source of the error is the limited data about the membrane microstructure.
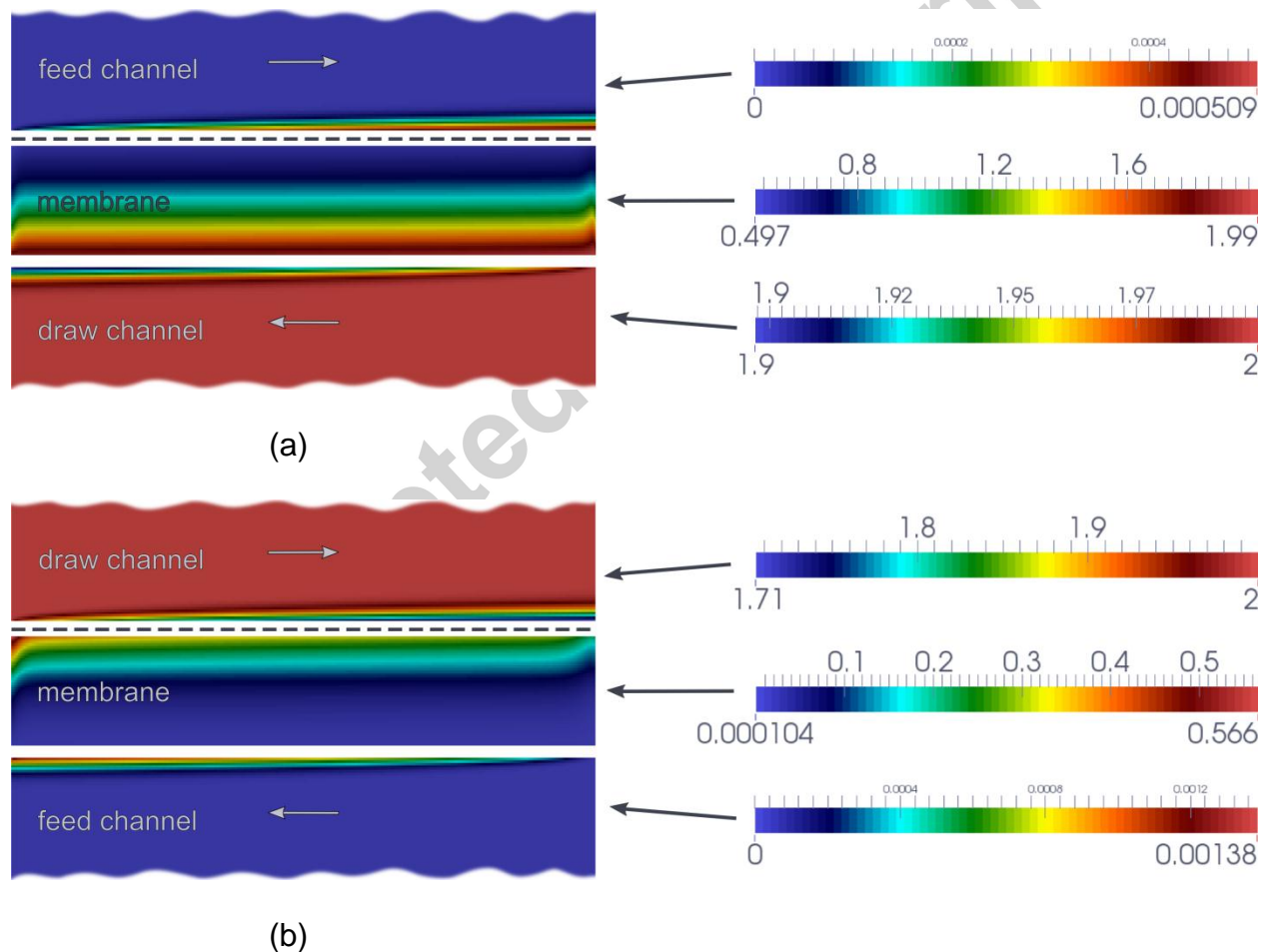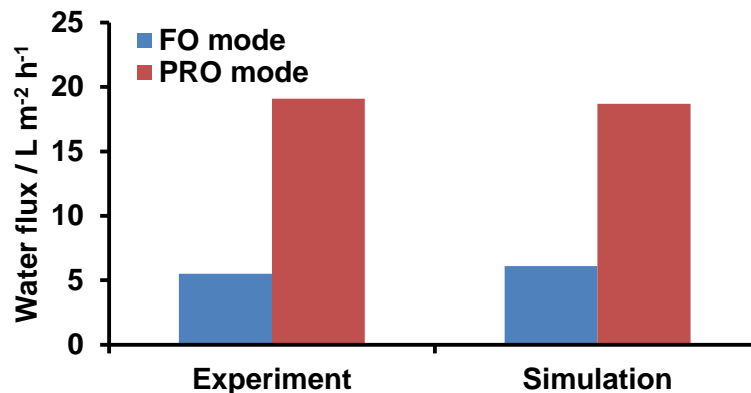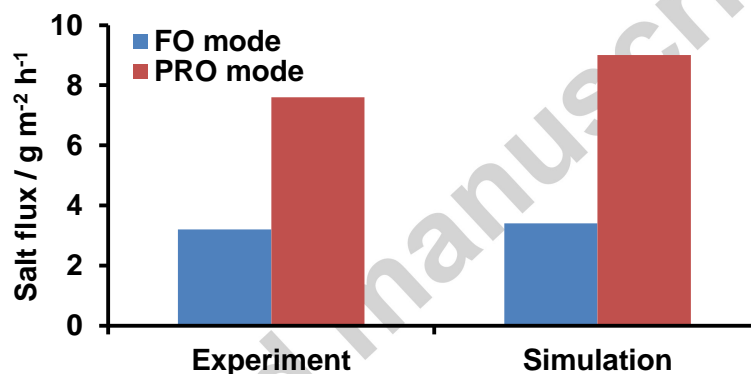

(a)

(b)

Figure 10. Concentration distributions for (a) FO and (b) PRO mode.

(a)

(b)

Figure 11. Comparison between experimental and simulated values of (a) water and (b) salt fluxes.

5 Conclusions

We propose a multi-scale simulation approach to model FO membranes with multi-layered homogeneous morphology and FO processes. We model PS-*b*-P4VP/IP membranes and validate the simulation results with experiments. The proposed simulation approach takes into account the microstructure of the membrane, which is

34

important for the internal concentration polarization and FO performance. Based on the simulation results, we conclude that the effective diffusivity needs careful treatment when modeling FO membranes and, by using our simulation approach, it can be accounted for accurately.

The proposed modeling approach opens new opportunities in the design of FO membranes. We demonstrate the modeling efficiency for a specific morphology, which we investigate experimentally in this work. However, we anticipate that the approach can be applied to the microstructures relevant for FO with different porosity, permeability, effective diffusivity, and thickness values. The simulations can be used for process optimization, particularly to choose the most adequate membrane morphology for a specific application. The approach used here is valid for systems without lateral macroscopic heterogeneity, e. g. is valid for membranes with sponge-like structure or regular nanosized cylinders. For membranes with larger heterogeneities, such as finger-like cavities, additional adjustments are still needed to provide a more realistic prediction, closer to the experimental results. Average parameters such as Darcy permeability and effective diffusivity from the micro-scale modeling can be fed into the macro-scale simulation, and the micro- and macro-scale processes can be considered separately. But averaging heterogeneities such as large finger-like cavities could introduce macroscopic effects, e.g. flow channeling, and deviate the modeling predictions from real experimental observations. More complex simulations are under consideration to extend the current approach to these membranes.

In the specific case investigated in this work we demonstrate that for FO performance not always the most permeable membrane is the most effective. The pore

morphology of the substrate can be more relevant, reducing the internal concentration polarization and finally leading to higher water flux. Therefore, block copolymer porous substrates with as uniform pore size on the surface, less tortuosity through the membrane, better pore interconnectivity, and high porosity were superior when compared to more common polysulfone substrates.

Acknowledgements

A

Δm

ρ

a

Δt

ΔP

R

C_p

C_f

B

$\Delta\pi$

J_w

J_s

C_t

C_0

V_t

V_0

$\mathbf{U}$

μ

P

K

K_s

Q

L

D

D_{eff}

C

ΔC

μ_{eff}

$\mathbf{n}$

l

π

Reference

[1] G.-D. Kang, Y.-M. Cao, Development of antifouling reverse osmosis membranes for water treatment: A review, Water Research, 46 (2012) 584-600.

[2] L. Zhao, P.C.-Y. Chang, W.W. Ho, High-flux reverse osmosis membranes incorporated with hydrophilic additives for brackish water desalination, Desalination, 308 (2013) 225-232.

[3] J.R. McCutcheon, R.L. McGinnis, M. Elimelech, A novel ammonia-carbon dioxide forward (direct) osmosis desalination process, Desalination, 174 (2005) 1-11.

[4] Z.-Y. Li, V. Yangali-Quintanilla, R. Valladares-Linares, Q. Li, T. Zhan, G. Amy, Flux patterns and membrane fouling propensity during desalination of seawater by forward osmosis, Water Research, 46 (2012) 195-204.

[5] A. Achilli, T.Y. Cath, E.A. Marchand, A.E. Childress, The forward osmosis membrane bioreactor: A low fouling alternative to MBR processes, Desalination, 239 (2009) 10-21.

[6] K.L. Hickenbottom, N.T. Hancock, N.R. Hutchings, E.W. Appleton, E.G. Beaudry, P. Xu, T.Y. Cath, Forward osmosis treatment of drilling mud and fracturing wastewater from oil and gas operations, Desalination, 312 (2013) 60-66.

[7] P.S. Zhong, N. Widjojo, T.-S. Chung, M. Weber, C. Maletzko, Positively charged nanofiltration (NF) membranes via uv grafting on sulfonated polyphenylenesulfone (SPPSU) for effective removal of textile dyes from wastewater, Journal of Membrane Science, 417 (2012) 52-60.

[8] S.P. Sun, T.A. Hatton, S.Y. Chan, T.-S. Chung, Novel thin-film composite nanofiltration hollow fiber membranes with double repulsion for effective removal of emerging organic matters from water, Journal of Membrane Science, 401 (2012) 152-162.

[9] Y. Han, Z. Xu, C. Gao, Ultrathin graphene nanofiltration membrane for water purification, Advanced Functional Materials, 23 (2013) 3693-3700.

[10] H. Maab, A. Al Saadi, L. Francis, S. Livazovic, N. Ghafour, G.L. Amy, S.P. Nunes, Polyazole hollow fiber membranes for direct contact membrane distillation, Industrial & Engineering Chemistry Research, 52 (2013) 10425-10429.

[11] A. Alkhudhiri, N. Darwish, N. Hilal, Membrane distillation: A comprehensive review, Desalination, 287 (2012) 2-18.

[12] P. Wang, M.M. Teoh, T.-S. Chung, Morphological architecture of dual-layer hollow fiber for membrane distillation with higher desalination performance, Water Research, 45 (2011) 5489-5500.

[13] A.G. Fane, R. Wang, M.X. Hu, Synthetic membranes for water purification: Status and future, Angewandte Chemie International Edition, 54 (2015) 3368-3386.

[14] T.-S. Chung, S. Zhang, K.Y. Wang, J. Su, M.M. Ling, Forward osmosis processes: Yesterday, today and tomorrow, Desalination, 287 (2012) 78-81.

[15] V. Sant'Anna, L.D.F. Marczak, I.C. Tessaro, Membrane concentration of liquid foods by forward osmosis: Process and quality view, Journal of Food Engineering, 111 (2012) 483-489.

[16] S.-F. Pan, M.-P. Zhu, J.P. Chen, Z.-H. Yuan, L.-B. Zhong, Y.-M. Zheng, Separation of tetracycline from wastewater using forward osmosis process with thin film composite

membrane-implications for antibiotics recovery, Separation and Purification Technology, 153 (2015) 76-83.

[17] M. Xie, M. Zheng, P. Cooper, W.E. Price, L.D. Nghiem, M. Elimelech, Osmotic dilution for sustainable greenwall irrigation by liquid fertilizer: Performance and implications, Journal of Membrane Science, 494 (2015) 32-38.

[18] N. Widjojo, T.-S. Chung, M. Weber, C. Maletzko, V. Warzelhan, The role of sulphonated polymer and macrovoid-free structure in the support layer for thin-film composite (TFC) forward osmosis (FO) membranes, Journal of Membrane Science, 383 (2011) 214-223.

[19] N.Y. Yip, A. Tiraferri, W.A. Phillip, J.D. Schiffman, M. Elimelech, High performance thin-film composite forward osmosis membrane, Environmental Science & Technology, 44 (2010) 3812-3818.

[20] G. Han, S. Zhang, X. Li, N. Widjojo, T.-S. Chung, Thin film composite forward osmosis membranes based on polydopamine modified polysulfone substrates with enhancements in both water flux and salt rejection, Chemical Engineering Science, 80 (2012) 219-231.

[21] J. Wei, C. Qiu, C.Y. Tang, R. Wang, A.G. Fane, Synthesis and characterization of flat-sheet thin film composite forward osmosis membranes, Journal of Membrane Science, 372 (2011) 292-302.

[22] Y. Yu, S. Seo, I.-C. Kim, S. Lee, Nanoporous polyethersulfone (PES) membrane with enhanced flux applied in forward osmosis process, Journal of Membrane Science, 375 (2011) 63-68.

[23] R. Wang, L. Shi, C.Y. Tang, S. Chou, C. Qiu, A.G. Fane, Characterization of novel forward osmosis hollow fiber membranes, Journal of Membrane Science, 355 (2010) 158-167.

[24] X. Song, Z. Liu, D.D. Sun, Nano gives the answer: Breaking the bottleneck of internal concentration polarization with a nanofiber composite forward osmosis membrane for a high water production rate, Advanced Materials, 23 (2011) 3256-3260.

[25] C. Klaysom, S. Hermans, A. Gahlaut, S. Van Craenenbroeck, I.F.J. Vankelecom, Polyamide/polyacrylonitrile (PA/PAN) thin film composite osmosis membranes: Film optimization, characterization and performance evaluation, Journal of Membrane Science, 445 (2013) 25-33.

[26] P.H.H. Duong, T.-S. Chung, Application of thin film composite membranes with forward osmosis technology for the separation of emulsified oil–water, Journal of Membrane Science, 452 (2014) 117-126.

[27] Y. Cui, Q. Ge, X.-Y. Liu, T.-S. Chung, Novel forward osmosis process to effectively remove heavy metal ions, Journal of Membrane Science, 467 (2014) 188-194.

[28] P.H.H. Duong, S. Chisca, P.-Y. Hong, H. Cheng, S.P. Nunes, T.-S. Chung, Hydroxyl functionalized polytriazole-co-polyoxadiazole as substrates for forward osmosis membranes, ACS Applied Materials & Interfaces, 7 (2015) 3960-3973.

[29] A. Tiraferri, N.Y. Yip, W.A. Phillip, J.D. Schiffman, M. Elimelech, Relating performance of thin-film composite forward osmosis membranes to support layer formation and structure, Journal of Membrane Science, 367 (2011) 340-352.

[30] L. Shi, S.R. Chou, R. Wang, W.X. Fang, C.Y. Tang, A.G. Fane, Effect of substrate structure on the performance of thin-film composite forward osmosis hollow fiber membranes, Journal of Membrane Science, 382 (2011) 116-123.
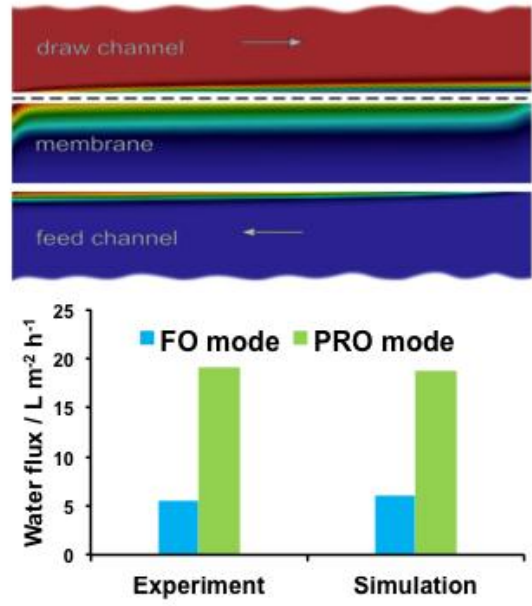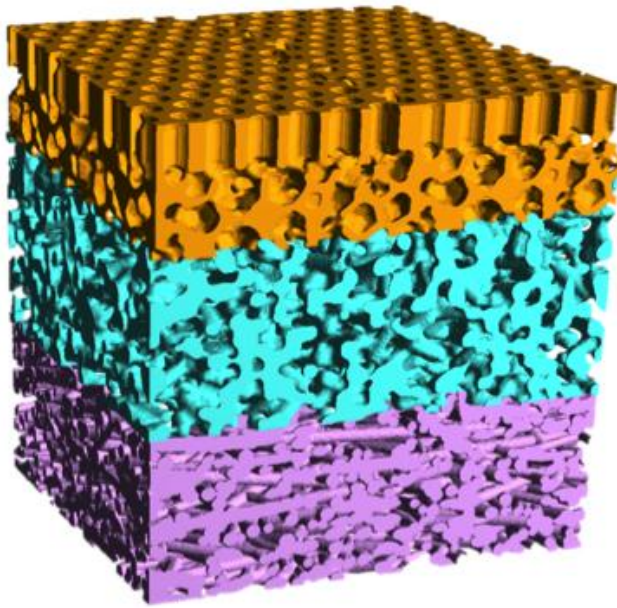
[31] L. Huang, J.R. McCutcheon, Impact of support layer pore size on performance of thin film composite membranes for forward osmosis, Journal of Membrane Science, 483 (2015) 25-33.

[32] L. Huang, J.T. Arena, S.S. Manickam, X. Jiang, B.G. Willis, J.R. McCutcheon, Improved mechanical properties and hydrophilicity of electrospun nanofiber membranes for filtration applications by dopamine modification, Journal of Membrane Science, 460 (2014) 241-249.

[33] V. Abetz, Isoporous block copolymer membranes, Macromolecular Rapid Communications, 36 (2015) 10-22.

[34] E.B. Gowd, M.S. Rama, M. Stamm, Nanostructures based on self-assembly of block copolymers, Springer, 2012.

[35] H.J. Fan, P. Werner, M. Zacharias, Semiconductor nanowires: From self-organization to patterned growth, Small, 2 (2006) 700-717.

[36] S.P. Nunes, R. Sougrat, B. Hooghan, D.H. Anjum, A.R. Behzad, L. Zhao, N. Pradeep, I. Pinnau, U. Vainio, K.-V. Peinemann, Ultraporous films with uniform nanochannels by block copolymer micelles assembly, Macromolecules, 43 (2010) 8079-8085.

[37] S.P. Nunes, M. Karunakaran, N. Pradeep, A.R. Behzad, B. Hooghan, R. Sougrat, H. He, K.-V. Peinemann, From micelle supramolecular assemblies in selective solvents to isoporous membranes, Langmuir, 27 (2011) 10184-10190.

[38] P. Madhavan, R. Sougrat, A.R. Behzad, K.-V. Peinemann, S.P. Nunes, Ionic liquids as self-assembly guide for the formation of nanostructured block copolymer membranes, Journal of Membrane Science, 492 (2015) 568-577.

[39] H. Yu, X. Qiu, N. Moreno, Z. Ma, V.M. Calo, S.P. Nunes, K.V. Peinemann, Self-assembled asymmetric block copolymer membranes: Bridging the gap from ultra- to nanofiltration, Angewandte Chemie International Edition, 54 (2015) 13937-13941.

[40] X. Qiu, H. Yu, M. Karunakaran, N. Pradeep, S.P. Nunes, K.-V. Peinemann, Selective separation of similarly sized proteins with tunable nanoporous block copolymer membranes, ACS Nano, 7 (2012) 768-776.

[41] M.M. Pendergast, E.M. Hoek, A review of water treatment membrane nanotechnologies, Energy & Environmental Science, 4 (2011) 1946-1971.

[42] M. Shi, G. Printsypar, O. Iliev, V.M. Calo, G.L. Amy, S.P. Nunes, Water flow prediction for membranes using 3D simulations with detailed morphology, Journal of Membrane Science, 487 (2015) 19-31.

[43] K. Lee, R. Baker, H. Lonsdale, Membranes for power generation by pressure-retarded osmosis, Journal of Membrane Science, 8 (1981) 141-171.

[44] S. Loeb, L. Titelman, E. Korngold, J. Freiman, Effect of porous support fabric on osmosis through a Loeb-Sourirajan type asymmetric membrane, Journal of Membrane Science, 129 (1997) 243-249.

[45] C.Y. Tang, Q. She, W.C. Lay, R. Wang, A.G. Fane, Coupled effects of internal concentration polarization and fouling on flux behavior of forward osmosis membranes during humic acid filtration, Journal of Membrane Science, 354 (2010) 123-133.

[46] M. Park, J.J. Lee, S. Lee, J.H. Kim, Determination of a constant membrane structure parameter in forward osmosis processes, Journal of Membrane Science, 375 (2011) 241-248.

[47] G.Z. Ramon, E.M. Hoek, Transport through composite membranes, part 2: Impacts of roughness on permeability and fouling, Journal of Membrane Science, 425 (2013) 141-148.

[48] G.Z. Ramon, M.C. Wong, E.M. Hoek, Transport through composite membrane, part 1: Is there an optimal support membrane?, Journal of Membrane Science, 415 (2012) 298-305.

[49] W. Li, Y. Gao, C.Y. Tang, Network modeling for studying the effect of support structure on internal concentration polarization during forward osmosis: Model development and theoretical analysis with fem, Journal of Membrane Science, 379 (2011) 307-321.

[50] A. Sagiv, R. Semiat, Finite element analysis of forward osmosis process using NaCl solutions, Journal of Membrane Science, 379 (2011) 86-96.

[51] The virtual material laboratory geodict, http://www.geodict.com, 2014.

[52] V.M. Calo, O. Iliev, Z. Lakdawala, K. Leonard, G. Printsypar, Pore-scale modeling and simulation of flow, transport, and adsorptive or osmotic effects in membranes: The influence of membrane microstructure, International Journal of Advances in Engineering Sciences and Applied Mathematics, 7 (2015) 2-13.

[53] P. Neelakanda, E. Barankova, K.-V. Peinemann, Polymer supported ZIF-8 membranes by conversion of sputtered zinc oxide layers, Microporous and Mesoporous Materials, 220 (2016) 215-219.

[54] H.K. Lonsdale, Recent advances in reverse osmosis membranes, Desalination, 13 (1973) 317-332.

[55] K.Y. Wang, R.C. Ong, T.-S. Chung, Double-skinned forward osmosis membranes for reducing internal concentration polarization within the porous sublayer, Industrial & Engineering Chemistry Research, 49 (2010) 4824-4831.

[56] S. Livazovic, Z. Li, A. Behzad, K.-V. Peinemann, S.P. Nunes, Cellulose multilayer membranes manufacture with ionic liquid, Journal of Membrane Science, 490 (2015) 282-293.

[57] X. Li, K.Y. Wang, B. Helmer, T.-S. Chung, Thin-film composite membranes and formation mechanism of thin-film layers on hydrophilic cellulose acetate propionate substrates for forward osmosis processes, Industrial & Engineering Chemistry Research, 51 (2012) 10039-10050.

[58] A.K. Ghosh, E.M.V. Hoek, Impacts of support membrane structure and chemistry on polyamide–polysulfone interfacial composite membranes, Journal of Membrane Science, 336 (2009) 140-148.

[59] S. Karan, Z. Jiang, A.G. Livingston, Sub-10 nm polyamide nanofilms with ultrafast solvent transport for molecular separation, Science, 348 (2015) 1347-1351.

[60] S.J. Vanhook, M.F. Schatz, J. Swift, W. McCormick, H.L. Swinney, Long-wavelength surface-tension-driven bénard convection: Experiment and theory, Journal of Fluid Mechanics, 345 (1997) 45-78.

Highlights

- A multi-scale simulation approach to model forward osmosis processes

- Micro-scale model for homogeneous layered microstructure of the substrate

- Macro-scale model for FO cross-flow setups

- Block copolymer membrane as an FO substrate

Graphical abstract